Article

Design and Optimize the Performance of Self-Powered Photodetector Based on PbS/TiS$_3$ Heterostructure by SCAPS-1D

Huizhen Yao and Lai Liu *

Key Laboratory of Instrumentation Science and Dynamic Measurement, Ministry of Education,
School of Instrument and Electronics, North University of China, Taiyuan 030051, China; huizhenyao@126.com
* Correspondence: liulaiopto@163.com

Abstract: Titanium trisulphide (TiS$_3$) has been widely used in the field of optoelectronics owing to its superb optical and electronic characteristics. In this work, a self-powered photodetector using bulk PbS/TiS$_3$ p-n heterojunction is numerically investigated and analyzed by a Solar Cell Capacitance Simulator in one-Dimension (SCAPS-1D) software. The energy bands, electron-holes generation or recombination rate, current density-voltage (J-V), and spectral response properties have been investigated by SCAPS-1D. To improve the performance of photodetectors, the influence of thickness, shallow acceptor or donor density, and defect density are investigated. By optimization, the optimal thickness of the TiS$_3$ layer and PbS layer are determined to be 2.5 μm and 700 nm, respectively. The density of the superior shallow acceptor (donor) is 10^{15} (10^{22}) cm^{-3}. High quality TiS$_3$ film is required with the defect density of about 10^{14} cm^{-3}. For the PbS layer, the maximum defect density is 10^{17} cm^{-3}. As a result, the photodetector based on the heterojunction with optimal parameters exhibits a good photoresponse from 300 nm to 1300 nm. Under the air mass 1.5 global tilt (AM 1.5G) illuminations, the optimal short-circuit current reaches 35.57 mA/cm^2 and the open circuit voltage is about 870 mV. The responsivity (R) and a detectivity (D*) of the simulated photodetector are 0.36 A W^{-1} and 3.9×10^{13} Jones, respectively. The simulation result provides a promising research direction to further broaden the TiS$_3$-based optoelectronic device.

Keywords: simulation; TiS$_3$/PbS; heterostructure; photodetector; SCAPS-1D

1. Introduction

Photodetectors that directly convert light into electrical signals have been developed for numerous applications, including medical diagnosis, aviation, target recognition, missile warning, and other fields [1–7]. Recently, self-powered photodetectors which can realize light detection without an external power supply have aroused a great deal of interest. The self-powered devices can work independently because of the photoelectric effect based on p–n or Schottky junction under illumination from light sources [8]. The built-in electric field existing in effective heterojunction between different materials will function as a driving force for high efficiency photogenerated carriers' separation and produce continuous photocurrent. Photodetectors with self-powered behaviors based on p–n junction exhibit outstanding photoelectric performance, such as high response speed, large linear region, and low noise, and have achieved significant progresses [9].

Titanium trisulphide (TiS$_3$) with a monoclinic structure is an n-type semiconducting material which has a direct optical bandgap of 1.0 eV [10,11]. Theoretically, TiS$_3$ will be a potential candidate substitution to silicon, micro or nanostructured, due to its exceptional carrier mobility (as high as ~10^4 cm^2 V^{-1} s^{-1}), high anisotropy, high optical absorption coefficient, and high chemical stability in the open-air [12,13]. Typically, the TiS$_3$ nanoribbon material has been successfully obtained in laboratory by sulfuration of Ti film. The unique optoelectronics properties of TiS$_3$ nanostructure make it wildly useful in the fields of cathodes in batteries [14,15], hydrogen storage [16,17], thermoelectric energy conversion

devices [18–20], and optoelectronics applications [21–24]. Niu et al. have developed a mixed-dimensionality TiS$_3$/Si n–p heterostructure broadband photodetector via staking an n-type TiS$_3$ nanoribbon onto p-type silicon substrate. The photoresponse of the device strongly depends on the polarization direction of the illumination. The high responsivity and on/off ratio of the TiS$_3$/Si device were ascribed to the improvement in charge separation coming from the coupling effect of TiS$_3$ nanoribbon and Si substrate [25]. Frisenda et al. have fabricated TiS$_3$-based nanoribbon photodetectors by the dielectrophoresis method between two gold electrodes. The photodetector can work efficiently in the visible region and possesses a responsivity of 3.8 mA/W [26]. Huang et al. synthesized TiS$_3$ nanoribbon array film on Ti-coated glass-carbon substrate by using a chemical vapor transport method. The vertically grown TiS$_3$ film with moderate S$_2{}^{2-}$ vacancies exhibits a long electron diffusion length for collecting electrons efficiently and an outstandingly high photocurrent density of 15.35 mA/cm^2 was achieved at 1.4 V versus using reversible hydrogen electrode [27]. The TiS$_3$ film has been proven as an excellent photoanode material. However, there are few reports concerning the self-powered photodetector using the TiS$_3$ film.

In this work, a self-powered PbS/TiS$_3$ p–n heterojunction film photodetector is numerically investigated and analyzed by one-Dimension software SCAPS-1D. By numerically modeling, the impact of thickness, defect density, and shallow acceptor or donor density on the performance of photodetectors were investigated. Under standard AM 1.5G illuminations, the achieved responsivity value is 0.36 A W^{-1} and the detectivity value is 3.9 × 10^{13} Jones of the photodetectors. The photodetector based on the heterojunction with optimal parameters exhibits a broad photoresponse in the UV-visible and near-infrared light region. The simulation result provides a promising research direction to further broaden the TiS$_3$-based optoelectronic device.

2. Numerical Simulation and Device Structure

The numerical simulation software used in this work is SCAPS-1D (V3.3.07), developed by the Department of Electronics and Information Systems of the Gent University (Ghent, Belgium) [28,29]. The software has been extensively used for simulating the thin-film solar cells to explore the electrical and optical properties, as well as the physics involved. As per previous reports, the simulated results from SCAPS have a good agreement with the experimental results [30,31]. In recent years, a number of research works based on SCAPS-1D software explored its applications in finding highly efficient photovoltaic devices [32–37]. Fundamentally, SCAPS-1D solves three sets of equations, Poisson's equation, hole continuity, and electron continuity under the constraint of boundary conditions. These three equations are shown below [38–40]:

$$\frac{\partial^2 \varphi}{\partial x^2} + \frac{q}{\varepsilon}[p(x) - n(x) - \rho_n + \rho_p - N_A + N_D] = 0 \tag{1}$$

$$\frac{1}{q}\frac{dJ_p}{dx} = G_{\mathrm{op}}(x) - R(x) \tag{2}$$

$$\frac{1}{q}\frac{dJ_{\mathrm{n}}}{dx} = G_{\mathrm{op}}(x) + R(x) \tag{3}$$

where φ shows the electrostatic potential, ε is the dielectric constant, and q is the electron charge. N_A is acceptor type and N_D is donor type density, respectively. $p(n)$ is hole (electron) concentration. ρ_p (ρ_n) is hole (electron) distribution. J_p is the current densities of the hole and J_{n} is the current densities of the electron, respectively. G_{op} designates the optical generation rate and R is the net recombination including direct and indirect recombination. All of these parameters are the function of the position coordinate x.

The numerical modeling is an important step to understand the physical properties of, and to realize, the highly efficient photoelectronic device. The narrow band gap TiS$_3$ layer acts as an absorber. The fluorine-doped tin oxide (FTO) layer is employed as a transparent conductive oxide layer. Figure 1a shows the diagrammatic drawing of the

FTO/ PbS/TiS$_3$/Ag thin-film heterojunction architecture photodetector. The PbS/TiS$_3$ heterojunctions are constructed in the designed device. The energy band scheme for the PbS/TiS$_3$ heterojunction thin-film photodetector is shown in Figure 1b. It is clearly observed that the conduction band of the PbS layer is about 0.6 eV higher compared with that of the TiS$_3$ layer. The conduction band offset would promote photo-generated electrons towards the Ag electrode. Furthermore, the valence band maximum of the TiS$_3$ layer is very close to that of the PbS. The estimated valance band offset is ~0.2 eV at the PbS/TiS$_3$ interface, which would promote photo-generated holes' transport to the FTO substrate.
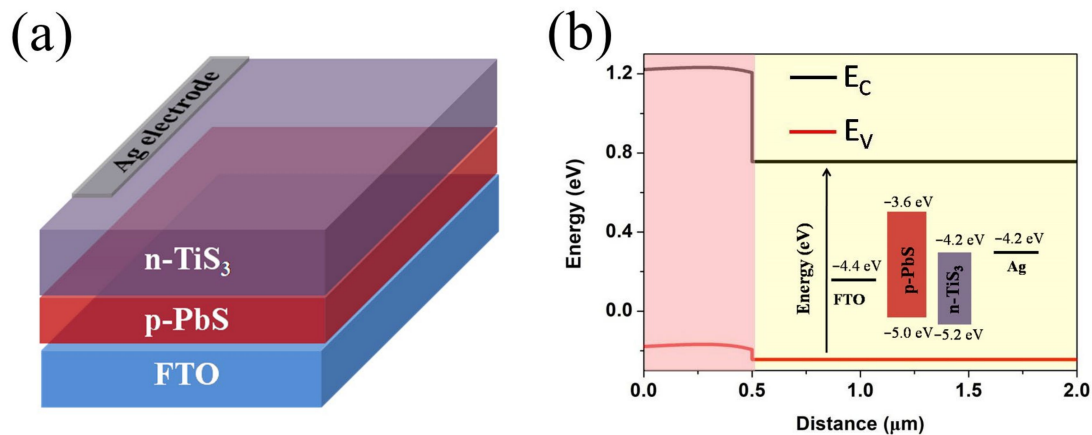

Figure 1. (**a**) Schematic n-TiS$_3$/p-PbS heterostructure photodetector, (**b**) energy band scheme of PbS/TiS$_3$ heterojunction.

The physical parameters of PbS and TiS$_3$ layers used in this simulation are shown in Table 1. All these parameters are from previous reports and theories [12,41–43]. The approximate thermal velocity of electrons and holes in PbS and TiS$_3$ semiconductor at room temperature is set at 10^7 cm/s for simplifying the numerical calculation. The surface recombination velocity of both electrons and holes at the FTO or Ag electrode is assumed to be 10^7 cm/s. The capture cross-sections of both the electron and hole are fixed at 10^{-14} cm^2. The interface defect parameters used in the PbS/TiS$_3$ heterojunction device simulation was 10^{12} cm^{-3}. AM 1.5G illuminations is used in all of our tests to optimize the simulation investigation, using 1000 W/m^2 from the PbS layer side. Photoresponsivity (R) and photodetectivity (D*) are important parameters for assessing the performance of a device and evaluate the detector sensitivity. It is assumed that the shot noise from the dark current is the primary source of total noise, R and D* are given as [44,45]:

$$R = \frac{I_{\text{light}}}{P_{in}S} \tag{4}$$

$$D^* = \frac{RS^{1/2}}{(2eI_d)^{1/2}} \tag{5}$$

where P_{in} is the incident light intensity, S represents the effective area of the device, and e is the elementary charge ($e = 1.60 \times 10^{-19}$ C).

Table 1. Parameters set for the simulation of TiS$_3$-based photodetector.

Properties	FTO	PbS	TiS$_3$
Thickness (nm)	300	200	500
Band gap (eV)	3.6	1.4	1.0
Electron affinity (eV)	4.0	4.35	4.8
Dielectric permittivity (relative)	9.0	10	9.98
Electron thermal velocity (cm/s)	1×10^7	1×10^7	1×10^7
Hole thermal velocity (cm/s)	1×10^7	1×10^7	1×10^7
CB effective DOS (cm^{-3})	2.2×10^{18}	1×10^{18}	1×10^{18}
VB effective DOS (cm^{-3})	1.8×10^{19}	1×10^{18}	1.8×10^{19}
Donor density N$_D$ (cm^{-3})	1×10^{17}	0	1×10^{18}
Acceptor density N$_A$ (cm^{-3})	0	1×10^{17}	0
Electron Mobility (cm^2/Vs)	100	50	200
Hole mobility (cm^2/Vs)	25	10	94

3. Results and Discussion

3.1. Influence of p-PbS and n-TiS$_3$ Layer Thickness on Device Performance

The thicknesses of n-TiS$_3$ and p-PbS layers are a key parameter to determine the performance of the detector. Optimizing the factor is in favor of obtaining optimal device performance. Figure 2 depicts the effect of the PbS and TiS$_3$ layer thickness on the suggested photodetector performance. The PbS layer thickness was modified between 0.1–1.7 µm, while keeping the thickness of the TiS$_3$ layer constant at 0.5 µm. As shown in Figure 2a,b, with the thickness of the PbS layer increasing from 0.1 µm to 0.7 µm, the short circuit photocurrent (J$_{SC}$) obviously increased from 14.33 to 30.21 mA/cm^2. This is attributed to the fact that the ultra-thin PbS layer leads to a large leakage current. However, as the thickness continues to rise to 900 nm, the J$_{SC}$ begins to decrease. When the thickness of the PbS layer was 1.7 µm, the J$_{SC}$ sharply reduced to 13.21 mA/cm^2. This resulted from a large number of photons being absorbed by the PbS layer and, thus, a smaller number of photons being able to reach the junction between PbS and TiS$_3$, which, in turn, reduced the generation of photogenerated carriers. Figure 2b shows that the variation trend of open circuit voltage (V$_{OC}$) is similar to that of J$_{SC}$. The appropriate thickness of the PbS layer means a higher carriers concentration, which can expand the depleted region of TiS$_3$ and enhance the performance. When the thickness of the PbS layer was 0.7 µm, the responsitivity and detectivity were 0.3 A/W and 3.3×10^{13} Jones (shown in Figure 2c), respectively. The results indicate that the optimum thickness of the PbS layer is 0.7 µm.

To investigate the effect of TiS$_3$ layer thickness, the simulation study was carried out with a thickness range from 0.1 µm to 4 µm as displayed in Figure 2d–f. It has been observed that the V$_{OC}$ and J$_{SC}$ of the simulated device were enhanced with increasing thickness of the TiS$_3$ layer. When the thickness of the TiS$_3$ layer was 0.1 µm, the photocurrent was 30.68 mA/cm^2. The thin TiS$_3$ layer could not fully absorb the incoming light resulting in low photocurrent while almost all of the photogenerated electron-hole could reach the corresponding electrode. As the thickness of the TiS$_3$ layer rises, more photons are captured, resulting in a rise in J$_{SC}$. The photocurrent increased to 35.53 mA/cm^2 with the thickness of the TiS$_3$ layer at 2.5 µm. Nevertheless, there was no significant change in the performance parameters when continuing to increase the thickness, resulting from the light absorption being saturated. The propagation path for the photo-generated carriers is long, leading to an increasing carrier recombination rate in the inner of TiS$_3$ layer. The simulated device can produce a highly efficient performance when the TiS$_3$ layer thickness is equal to 2.5 µm. The J–V characteristic curves for varying the PbS layer thickness with the constant optimized TiS$_3$ layer at 2.5 µm are also given in Figure S1 (Supporting Information). The tendency is similar to that in Figure 2a, which verifies our conclusion. The responsivity and detectivity are 0.36 A/W and 3.9×10^{13} Jones (shown in Figure 2f), respectively.
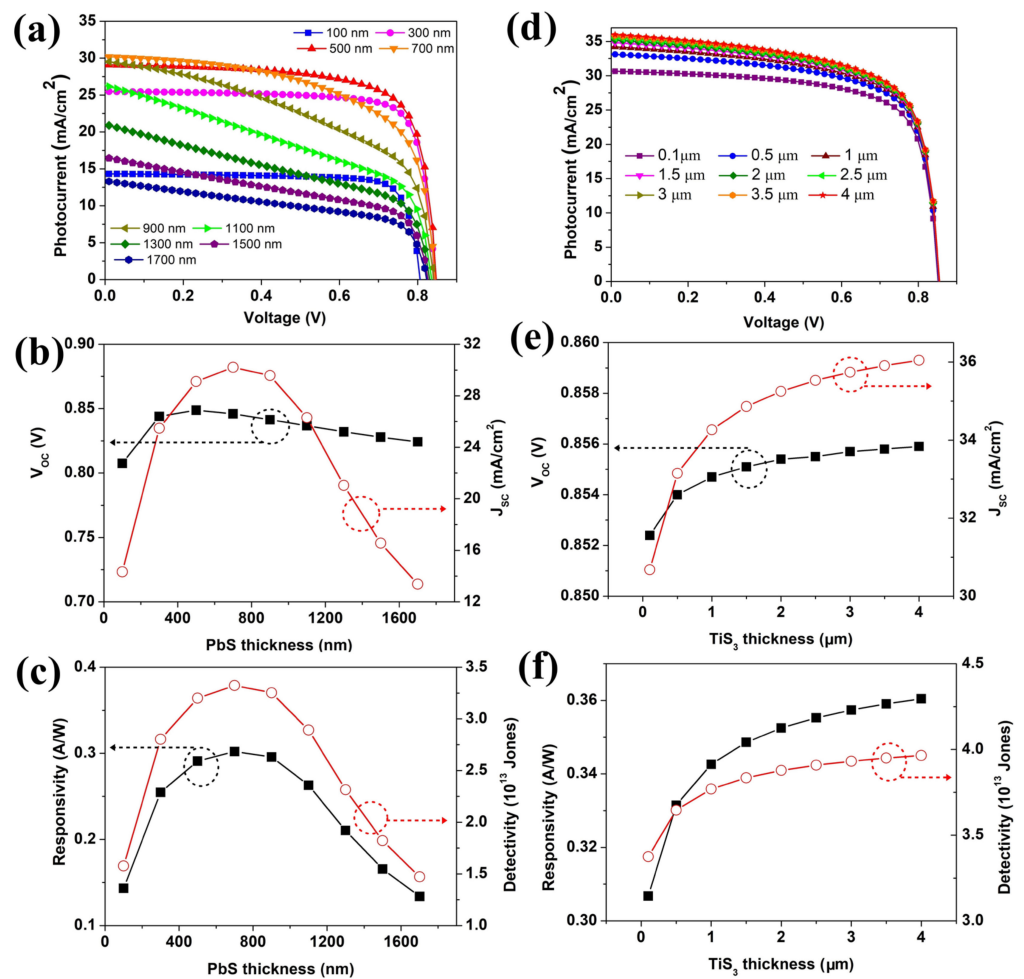
Figure 2. (**a**) J–V characteristic curves for varying the PbS layer thickness, (**b**) V_{OC} and J_{SC} variation, (**c**) R and D* variation with respect to the thickness of the PbS layer, (**d**) J–V characteristic curves for varying the TiS$_3$ layer thickness, (**e**) V_{OC} and J_{SC} variation, (**f**) R and D* variation with respect to the thickness of the TiS$_3$ layer.

3.2. Influence of Doping Concentration of p-PbS Layer and n-TiS$_3$ Layer

Shallow acceptor density (N_A) plays an important role in improving the performance of photodetectors. In the simulation study, the doping concentration of the PbS layer was varied from 10^{12} cm^{-3} to 10^{19} cm^{-3}, while other parameters remained the same. It is shown in Figure 3a,b that the V_{OC} and J_{SC} improves with the concentration of the PbS carrier concentration rising but below 10^{15} cm^{-3}, indicating that the minority charge carrier recombination was reducing. When the doping density of the PbS layer continually increased to 10^{17} cm^{-3}, the overall performance of the photodetector including J_{SC}, V_{OC}, responsivity, and detectivity were quenched enormously due to the increased carriers recombination, as shown in Figure S2 (Supporting Information). It is observed in Figure 3c that the maximum responsivity and detectivity are 0.29 A/W and 3.2×10^{13} Jones when the acceptor density is at 10^{15} cm^{-3}. The results suggest that the proper doping of the PbS layer results in a more efficient performance. As shown in Figure 3d,e, the donor density (N_D) of the TiS$_3$ layer is ranging from 10^{14} to 10^{22} cm^{-3}. It can be observed that all the performances of the simulated photodetector were enhanced with the increasing doping density of the TiS$_3$ layer. It is concluded that the high doping density results in a large built-in potential at the PbS/TiS$_3$ interface. Consequently, the photo-generated carrier recombination is observably inhibited. In the numerical study, the doping concentration of 10^{22} cm^{-3} is chosen to obtain the best responsivity and detectivity (as shown in Figure 3f) of the designed photodetector.
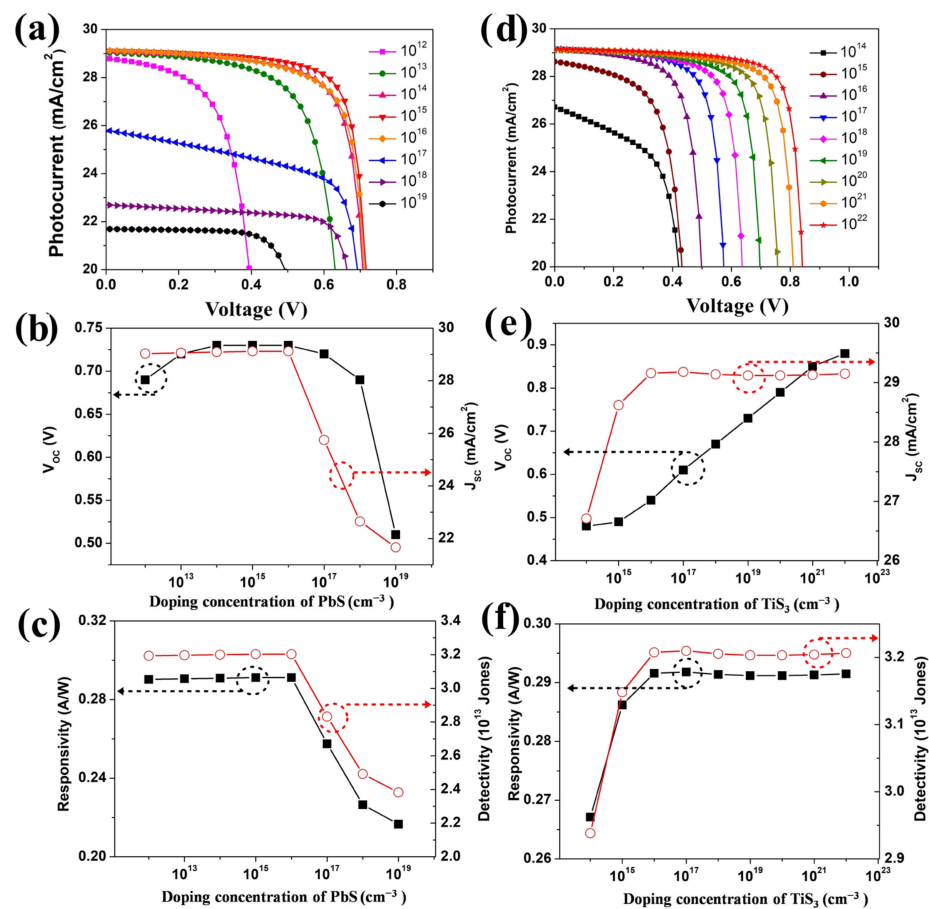
Figure 3. (**a**) J–V characteristic curves, (**b**) V_{OC} and J_{SC} variation, (**c**) R and D* variation for varying the PbS shallow acceptor density, (**d**) J–V characteristic curves, (**e**) V_{OC} and J_{SC} variation, (**f**) R and D* variation for varying the TiS$_3$ shallow donor density.

3.3. Influence of the Concentration of Defect Density

The performance of the device is also dependent on the defect density of each layer. The increase in defect density results in more photo-generated carrier recombination, which seriously reduces the efficiency of the device. In the study, the defect density of the PbS layer and TiS$_3$ layer are varied in the range of 10^{12}–10^{22} cm^{-3} and 10^{12}–10^{20} cm^{-3}, respectively. When the defect density of PbS was set from 10^{12} to 10^{17}, shown in Figure S3 (Supporting Information), the photoelectric performance of the simulated photodetector had little change. It is seen from Figure 4a,b that, given a continuous augment in the defect density of the PbS layer, V_{OC} and J_{SC} are degraded. When the defect density of the PbS layer increased to 10^{22} cm^{-3}, the J_{SC} reduced to 22.24 mA/cm^2 and the corresponding responsivity quenched to 0.22 A/W, as shown in Figure 4c. This is attributed to the raised carrier recombination rate with the localized energy levels created by the defects. The results show that only a mass concentration of defects in the PbS layer quenched the performance of the device. The optimal defect density of the PbS layer is ranged from 10^{12} to 10^{17}. As shown in Figure S4 (Supporting Information), when the defect density of the TiS$_3$ is ranged from 10^{12} to 10^{14}, the photocurrent is kept at around 29.38 mA/cm^2. When the defect density was magnified from 10^{14} cm^{-3} to 10^{20} cm^{-3}, shown in Figure 4d,e, J_{SC} varied from 29.38 mA/cm^2 to 21.45 mA/cm^2. It is observed from Figure 4f that responsivity and detectivity had a similar downtrend. The optimal responsivity and detectivity are 0.29 A/W and 3.2×10^{13} Jones, when the defect density of the PbS layer and TiS$_3$ layer are ranged from 10^{12} cm^{-3} to 10^{17} cm^{-3} and from 10^{12} to 10^{14} cm^{-3}.
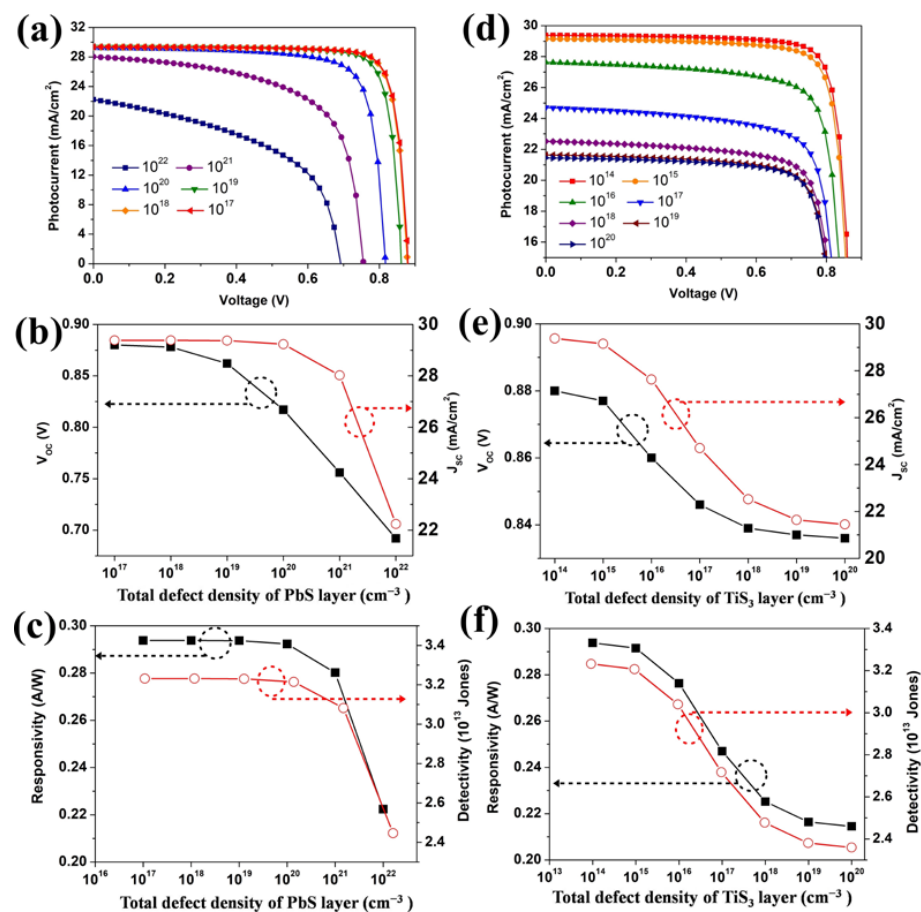
Figure 4. (**a**) J–V characteristic curves for varying the PbS defect density, (**b**) V_{OC} and J_{SC} variation, (**c**) R and D* variation with respect to the PbS defect density of the PbS layer, (**d**) J–V characteristic curves for varying the TiS₃ defect density, (**e**) V_{OC} and J_{SC} variation, (**f**) R and D* variation with respect to the defect density of the TiS₃ layer.

3.4. Self-Powered n-TiS₃/p-PbS Heterostructure Photodetector

Through simulated optimizing, the thickness of the TiS₃ layer and PbS layer are 2.5 μm and 700 nm, respectively. The density of the acceptor or donor is set at 10^{15} or 10^{22} cm^{-3}. The high quality TiS₃ film is required to have a defect density of about 10^{14} cm^{-3}. For the PbS layer, the maximum defect density is 10^{17} cm^{-3}. The optoelectronic performances of the simulated n-TiS₃/p-PbS heterostructure devices in dark and AM 1.5G standard illuminations are shown in Figure 5a. In the dark, the photodetector displays a typical rectifying I–V characteristic due to the heterostructure formed at the interface between the n-TiS₃ and the p-PbS. Under AM 1.5G illuminations, an enhanced photocurrent is observed. The photocurrent of the simulated photodetector after majorization is 35.57 mA/cm². The optimal photoresponsivity of the proposed heterostructure device is about 0.36 A W^{-1} and the corresponding detectivity is 3.9×10^{13} Jones, which is comparable with the photodetector based on nanostructured silicon [46,47]. The ratio of light and dark current (I_{light}/I_{dark}) is about 10^{14} at bias voltages of 0 V. This phenomenon suggests that the photodetector can be triggered by itself. The built-in electric field which formed at the TiS₃ and PbS interface can separate the photogenerated carriers even at zero bias. The photoelectrical properties displayed by the TiS₃–PbS device can be clarified by the band scheme of the PbS and TiS₃ materials, as displayed in Figure 5b. The band gap energies of TiS₃ and PbS semiconductors are about 1.0 and 1.4 eV, respectively. As for the insulate layer, the different inherent nature leads to a different position of the Fermi levels (Supporting Information Figure S5). The electrons at the interface will be transported from the high level to the lower and, in turn, produce a potential difference at the contact interface. This phenomenon is displayed in

the band scheme by the bending of the conduction and the valence band at the interface (as shown in Figure 5b). The rectifying I−V characteristics and the photovoltaic effect noticed in the proposed photodetector resulted from the type-II band mechanism. Figure 5c shows the photoresponsivity of the simulated PbS/TiS$_3$ photodetector device. The device shows different light response characteristics under different light wavelengths. A distinct responsivity ranged from the UV to the near-infrared region is observed, which indicates the excellent broadband performance of the photodetector. With 780 nm illumination, the photodetector shows superior responsibility, as shown in Figure 5d. Figure 5e shows the I−V characteristics of the simulated device upon illumination (with 780 nm of wavelength) with enhanced optical power. It is noted that the photocurrent enhances monotonically with the augmenting light power density. This phenomenon can be a result of the growing number of photogenerated carriers as the light intensity increases. On the contrary, the responsivity decreases (Figure 5f). The R values of the photodetectors are large under low light power density, indicating that the simulated photodetectors are very sensitive to weak light.
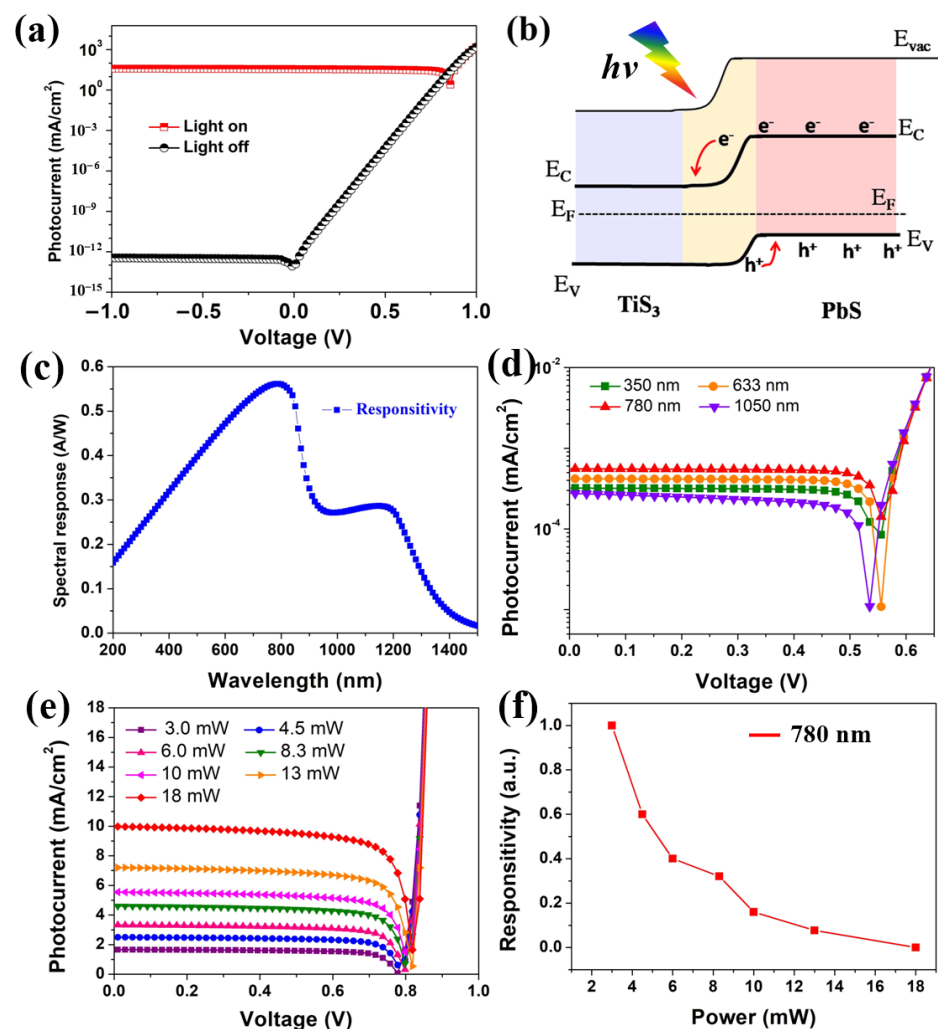

Figure 5. (**a**) I–V curves of the simulated photodetector with and without light illumination, (**b**) schematic band diagram after contacting, (**c**) responsivity with different illumination wavelengths at a power of 100 mW/cm^2, (**d**) I−V characteristics of simulated PbS/TiS$_3$ under different wavelengths of illumination and (**e**) illuminated with a 780 nm wavelength at different powers, (**f**) dependence of responsivity of the photodetector versus the light illumination power.

4. Conclusions

In summary, a self-powered PbS/TiS$_3$ heterostructure photodetector is numerically investigated. Herein, the PbS/TiS$_3$ photodetector is modeled and optimized using SCAPS-1D software. The important parameters, including the energy bands, electron-holes generation or recombination rate, current density–voltage (J–V), and spectral response properties of the proposed device, have been explored. The influence of thickness, shallow acceptor or donor density, and defect density are also investigated. As a result, the photodetector based on the heterojunction with optimal parameters exhibits a good photoresponse from 300 nm to 1300 nm. Under AM 1.5G illuminations, the optimal short-circuit current reaches 35.57 mA/cm^2 and the open circuit voltage is about 870 mV. The responsivity and a detectivity of the simulated photodetector are 0.36 A W^{-1} and 3.9×10^{13} Jones, respectively. The simulation result paves a promising way for further broadening the applicability of the TiS$_3$-based optoelectronic device.

Conflicts of Interest: The authors declare that there is no conflict of interests regarding the publication of this paper.

References

1. Wu, Z.; Zhai, C.; Kim, H.; Azoulay, D.; Ng, N. Emerging Design and Characterization Guidelines for Polymer-Based Infrared Photodetectors. *Acc. Chem. Res.* **2018**, *51*, 3144–3153. [CrossRef] [PubMed]
2. Liu, S.; Tian, J.; Wu, S.; Zhang, W.; Luo, M. A bioinspired broadband self-powered photodetector based on photo-pyroelectric-thermoelectric effect able to detect human radiation. *Nano Energy* **2021**, *93*, 106812. [CrossRef]
3. Jiao, Y.; Lu, G.; Feng, Y.; Zhang, C.; Wang, W.; Wu, Y.; Chen, M.; Ma, M.; Li, J.; Yang, L.; et al. Towards high sensitivity infrared detector using Cu$_2$Cd$_x$Zn$_{1-x}$SnSe$_4$ thin film by SCAPS simulation. *Sol. Energy* **2021**, *225*, 375–381. [CrossRef]
4. Clark, J.; Lanzani, G. Organic photonics for communications. *Nat. Photon.* **2010**, *4*, 438–446. [CrossRef]
5. Zhang, J.; Itzler, M.A.; Zbinden, H.; Pan, J.-W. Advances in InGaAs/InP single-photon detector systems for quantum communication. *Light Sci. Appl.* **2015**, *4*, e286. [CrossRef]
6. Tan, L.; Mohseni, H. Emerging technologies for high performance infrared detectors. *Nanophotonics* **2018**, *7*, 169–197. [CrossRef]
7. Tian, W.; Wang, D.; Chen, L.; Li, L. Self-Powered Nanoscale Photodetectors. *Small* **2017**, *13*, 1701848. [CrossRef]
8. Zhang, Z.; Zhang, W.; Wei, Z.; Jiang, Q.; Deng, M.; Chai, W.; Zhu, D.; Zhang, F.; You, L.; Zhang, J. Dipole-templated homogeneous grain growth of CsPbIBr$_2$ films for efficient self-powered, all-inorganic photodetectors. *Sol. Energy* **2020**, *209*, 371–378. [CrossRef]
9. Long, M.; Wang, P.; Fang, H.; Hu, W. Progress, challenges, and opportunities for 2D material based photodetectors. *Adv. Funct. Mater.* **2019**, *29*, 1803807. [CrossRef]
10. Finkman, E.; Fisher, B. Electrical transport measurements in TiS$_3$. *Solid State Commun.* **1984**, *50*, 25–28. [CrossRef]
11. Ferrer, J.; Ares, R.; Clamagirand, M.; Barawi, M.; Sánchez, C. Optical properties of titanium trisulphide (TiS$_3$) thin films. *Thin Solid Film.* **2013**, *535*, 398–401. [CrossRef]
12. Dai, J.; Zeng, X. Titanium trisulfide monolayer: Theoretical prediction of a new direct-gap semiconductor with high and anisotropic carrier mobility. *Angew. Chem.* **2015**, *127*, 7682–7686. [CrossRef]
13. Tripathi, N.; Pavelyev, V.; Sharma, P.; Kumar, S.; Rymzhina, A.; Mishra, P. Review of titanium trisulfide (TiS$_3$): A novel material for next generation electronic and optical devices. *Mater. Sci. Semicon. Proc.* **2021**, *127*, 105699. [CrossRef]

14. Li, L.; Lu, Y.; Zhang, Q.; Zhao, S.; Hu, Z.; Chou, S.L. Recent progress on layered cathode materials for nonaqueous rechargeable magnesium batteries. *Small* **2021**, *17*, 1902767. [CrossRef]

15. Holleck, L.; Driscoll, R. Transition metal sulfides as cathodes for secondary lithium batteries—II. titanium sulfides. *Electrochim. Acta* **1977**, *22*, 647–655. [CrossRef]

16. Ferrer, J.; Maciá, D.; Carcelén, V.; Ares, R.; Sánchez, C. On the photoelectrochemical properties of TiS_3 films. *Energy Procedia* **2012**, *22*, 48–52. [CrossRef]

17. Barawi, M.; Flores, E.; Ferrer, I.J.; Ares, J.R.; Sánchez, C. Titanium trisulphide (TiS_3) nanoribbons for easy hydrogen photogeneration under visible light. *J. Mater. Chem. A* **2015**, *3*, 7959–7965. [CrossRef]

18. Zhang, J.; Liu, X.; Wen, Y.; Shi, L.; Chen, R.; Liu, H.; Shan, B. Titanium trisulfide monolayer as a potential thermoelectric material: A first-principles-based boltzmann transport study. *ACS Appl. Mater. Interfaces* **2017**, *9*, 2509–2515. [CrossRef]

19. Morozova, V.; Korobeinikov, V.; Kurochka, V.; Titov, N.; Ovsyannikov, V. Thermoelectric properties of compressed titanium and zirconium trichalcogenides. *J. Phys. Chem. C* **2018**, *122*, 14362–14372. [CrossRef]

20. Molina-Mendoza, A.J.; Barawi, M.; Biele, R.; Flores, E.; Ares, J.R.; Sánchez, C.; Rubio-Bollinger, G.; Agraït, N.; D'Agosta, R.; Ferrer, I.J. Electronic bandgap and exciton binding energy of layered semiconductor TiS_3. *Adv. Electron. Mater.* **2015**, *1*, 1500126. [CrossRef]

21. Island, O.; Buscema, M.; Barawi, M.; Clamagirand, M.; Ares, R.; Sánchez, C.; Ferrer, J.; Steele, A.; Zant, J.; Castellanos-Gomez, A. Ultrahigh photoresponse of few-layer TiS_3 nanoribbon transistors. *Adv. Opt. Mater.* **2014**, *2*, 641–645. [CrossRef]

22. Silva-Guillén, J.A.; Canadell, E.; Guinea, F.; Roldán, R. Strain tuning of the anisotropy in the optoelectronic properties of TiS_3. *ACS Photon.* **2018**, *5*, 3231–3237. [CrossRef]

23. Liu, L.; Cheng, Z.; Jiang, B.; Liu, Y.; Zhang, Y.; Yang, F.; Wang, H.; Yu, F.; Chu, K.; Ye, C. Optoelectronic Artificial Synapses Based on Two-Dimensional Transitional-Metal Trichalcogenide. *ACS Appl. Mater. Interfaces* **2021**, *13*, 30797–30805. [CrossRef] [PubMed]

24. Talib, M.; Tabassum, R.; Abid; Islam, S.S.; Mishra, P. Improvements in the performance of a visible–NIR photodetector using horizontally aligned TiS_3 nanoribbons. *ACS Omega* **2019**, *4*, 6180–6191. [CrossRef]

25. Niu, Y.; Frisenda, R.; Flores, E.; Ares, J.R.; Jiao, W.; Perez de Lara, D.; Sánchez, C.; Wang, G.; Ferrer, J.; Castellanos-Gomez, A. Polarization-Sensitive and Broadband Photodetection Based on a Mixed-Dimensionality TiS_3/Si p–n Junction. *Adv. Opt. Mater.* **2018**, *6*, 1800351. [CrossRef]

26. Lipatov, A.; Wilson, P.M.; Shekhirev, M.; Teeter, J.D.; Netusil, R.; Sinitskii, A. Few-layered titanium trisulfide (TiS_3) field-effect transistors. *Nanoscale* **2015**, *7*, 12291–12296. [CrossRef]

27. Tian, Z.; Guo, X.; Wang, D.; Sun, D.; Zhang, S.; Bu, K.; Zhao, W.; Huang, F. Enhanced charge carrier lifetime of TiS_3 photoanode by introduction of $S2^{2-}$ vacancies for efficient photoelectrochemical hydrogen evolution. *Adv. Funct. Mater.* **2020**, *30*, 2001286. [CrossRef]

28. Soedergren, S.; Hagfeldt, A.; Olsson, J.; Lindquist, S.-E. Theoretical models for theaction spectrum and the current-voltage characteristics of microporous semiconductor films in photoelectrochemical cells. *J. Phys. Chem.* **1994**, *98*, 5552–5556. [CrossRef]

29. Burgelman, M.; Nollet, P.; Degrave, S. Modelling polycrystalline semiconductor solar cells. *Thin Solid Films* **2000**, *361*, 527–532. [CrossRef]

30. Huang, L.; Sun, X.; Li, C.; Xu, R.; Xu, J.; Du, Y.; Wu, X.; Ni, J.; Cai, K.; Li, J.; et al. Electron transport layer-free planar perovskite solar cells: Further performance enhancement perspective from device simulation. *Sol. Energy Mater. Sol. Cells* **2016**, *157*, 1038–1047. [CrossRef]

31. Decock, K.; Zabierowski, P.; Burgelman, M. Modeling metastabilities in chalcopyrite-based thin film solar cells. *J. Appl. Phys.* **2012**, *111*, 43703. [CrossRef]

32. He, Y.; Xu, L.; Yang, C.; Guo, X.; Li, S. Design and Numerical Investigation of a Lead-Free Inorganic Layered Double Perovskite $Cs_4CuSb_2Cl_{12}$ Nanocrystal Solar Cell by SCAPS-1D. *Nanomaterials* **2021**, *11*, 2321. [CrossRef] [PubMed]

33. Karthick, S.; Velumani, S.; Bouclé, J. Experimental and SCAPS simulated formamidinium perovskite solar cells: A comparison of device performance. *Sol. Energy* **2020**, *205*, 349–357. [CrossRef]

34. Huang, C.H.; Chuang, W.J. Dependence of performance parameters of CdTe solar cells on semiconductor properties studied by using SCAPS-1D. *Vacuum* **2015**, *118*, 32–37. [CrossRef]

35. Basak, A.; Singh, U.P. Numerical modelling and analysis of earth abundant Sb_2S_3 and Sb_2Se_3 based solar cells using SCAPS-1D. *Sol. Energy Mater. Sol. Cells* **2021**, *230*, 111184. [CrossRef]

36. Islam, S.; Sobayel, K.; Al-Kahtani, A.; Islam, M.A.; Muhammad, G.; Amin, N.; Shahiduzzaman, M.; Akhtaruzzaman, M. Defect Study and Modelling of SnX3-Based Perovskite Solar Cells with SCAPS-1D. *Nanomaterials* **2021**, *11*, 1218. [CrossRef]

37. Kanoun, A.; Kanoun, B.; Merad, E.; Goumri-Said, S. Toward development of high-performance perovskite solar cells based on $CH_3NH_3GeI_3$ using computational approach. *Sol. Energy* **2019**, *182*, 237–244. [CrossRef]

38. Sobayel, K.; Shahinuzzaman, M.; Amin, N.; Karim, M.R.; Dar, M.A.; Gul, R.; Alghoul, M.A.; Sopiana, K.; Hasan, A.K.M.; Akhtaruzzaman, M. Efficiency enhancement of CIGS solar cell by WS_2 as window layer through numerical modelling tool. *Sol. Energy* **2020**, *207*, 479–485. [CrossRef]

39. Minbashi, M.; Ghobadi, A.; Ehsani, M.H.; Dizaji, H.R.; Memarian, N. Simulation of high efficiency SnS-based solar cells with SCAPS. *Sol. Energy* **2018**, *176*, 520–525. [CrossRef]

40. Buffière, M.; Harel, S.; Guillot-Deudon, C.; Arzel, L.; Barreau, N.; Kessler, J. Effect of the chemical composition of co-sputtered Zn (O, S) buffer layers on Cu (In, Ga) Se_2 solar cell performance. *Phys. Stat. Solidi* **2015**, *212*, 282–290. [CrossRef]

41.   Agarwal, A.; Qin, Y.; Chen, B.; Blei, M.; Wu, K.; Liu, L.; Shen, X.; Wright, D.D.; Green, M.D.; Zhuang, L.; et al. Anomalous isoelectronic chalcogen rejection in 2D anisotropic vdW $TiS_{3(1-x)}Se_{3x}$ trichalcogenides. *Nanoscale* **2018**, *10*, 15654–15660. [CrossRef]

42.   Torun, E.; Sahin, H.; Chaves, A.; Wirtz, L.; Peeters, F.M. Ab initio and semiempirical modeling of excitons and trions in monolayer TiS_3. *Phys. Rev. B* **2018**, *98*, 075419. [CrossRef]

43.   Chen, C.; Wang, L.; Gao, L.; Nam, D.; Li, D.; Li, K.; Zhao, Y.; Ge, C.; Cheong, H.; Song, H.; et al. 6.5% certified efficiency Sb_2Se_3 solar cells using PbS colloidal quantum dot film as hole-transporting layer. *ACS Energy Lett.* **2017**, *2*, 2125–2132. [CrossRef]

44.   Choi, W.; Cho, M.Y.; Konar, A.; Lee, J.H.; Cha, G.B.; Hong, S.C.; Kim, S.; Kim, Y.; Jena, D.; Joo, J.; et al. High-detectivity multilayer MoS_2 phototransistors with spectral response from ultraviolet to infrared. *Adv. Mater.* **2012**, *24*, 5832–5836. [CrossRef]

45.   Binda, M.; Iacchetti, A.; Natali, D.; Beverina, L.; Sassi, M.; Sampietro, M. High detectivity squaraine-based near infrared photodetector with nA/cm^2 dark current. *Appl. Phys. Lett.* **2011**, *98*, 073303. [CrossRef]

46.   Yu, H.; Shu, S.; Xiong, X.; Xie, Q. Simulation design and performance study of Graphene/Mg_2Si/Si heterojunction photodetector. *Appl. Phys. A* **2021**, *127*, 548. [CrossRef]

47.   Wu, E.; Wu, D.; Jia, C.; Wang, Y.; Yuan, H.; Zeng, L.; Xu, T.; Shi, Z.; Tian, Y.; Li, X. In situ fabrication of 2D WS_2/Si type-II heterojunction for self-powered broadband photodetector with response up to mid-infrared. *ACS Photon.* **2019**, *6*, 565–572. [CrossRef]